Check for
updates

Effects of Void Defects on Fracture Features and Tensile Strength of C/SiC Composites: an Image-based FEM Study

Qiubo Li[1] · Yihui Chen[1] · Yanfei Chen[1] · Shigang Ai[1] · Daining Fang[1]

© The Author(s), under exclusive licence to Springer Nature B.V. 2021

Abstract

Manufacturing defects in ceramic matrix composites (CMCs), such as voids, microcracks, etc., significantly affect the damage events and strength of the materials. This study aims to reveal the effect of void defects on the failure behavior and tensile strength of a plain-woven C/SiC composite. The mesoscopic architectures of the C/SiC composites are tested by micro-computed tomography. Based on the μ-CT images of the material, finite element models (IB-FEM) of the C/SiC composite are established with different void volume fractions and different void geometry. The tensile strength and fracture features of the C/SiC composites are calculated by using the IB-FEM. The effects of void volume fraction and geometry on failure behaviors and tensile strength of the C/SiC composites are investigated and discussed. This study is of great significance for further understanding the influence of defects on the mechanical behavior of CMCs.

Keywords Image-based finite element method · C/SiC composite · Void defect · Tensile strength

1 Introduction

Ceramic matrix composites (CMCs) are recognized as promising thermal protection materials for their remarkable high-temperature mechanical properties [1], which have been used in many spacecraft components [2–4]. Their mechanical behavior under thermo-mechanical coupled loads is an essential issue in mechanics and material science. Due to their unique material preparation process, CMCs inevitably have preparation defects, such as micro-cracks, voids, fiber breakage, folds, and so on. The internal defects can disturb the textile architecture of the composites, affecting stress distribution inside the materials under external load and induce the damage and failure of the materials. Therefore, it is crucial to study the damage evolution and reveal the failure mechanisms of the CMCs considering internal defects under external loads.

✉ Shigang Ai
  sgai@bit.edu.cn

[1] Institute of Advanced Structure Technology, Beijing Institute of Technology, Beijing 100081, China

As a critical research approach for composite materials, numerical simulation has unique advantages compared with experimental research. Numerical simulation can directly access the physical parameters in materials or structures, such as deformation, temperature, damage events, etc. [5, 6]. At the same time, it significantly reduces research costs. For composite material calculations, Represented Volume Element (RVE) models are widely used to investigate their mechanical properties [7–10] and damage behaviors [11–15]. As an important topic, the effects of internal defects have been the interest of many researchers [16–19]. Liu et al. [20, 21] used Delaunay based feature preserving rational Bezier triangles to subdivide geometric regions, which solved the continuity problem of special points in NURBS multi-patch interfaces or T-spline curves, and grid generation could be automated. In addition, the hermitage high ladder damage model is used to correct the non-physical grid dependence shown in the continuous damage analysis. A lot of numerical examples show that this method has obvious advantages in efficiency and precision. Liu et al. [22], under the framework of continuum damage mechanics is established to describe the fatigue load caused by the damage evolution model, put forward loop jump method is used to describe the fatigue damage and its yield strength related to loop and the associated flow rule, solved the predefined phases and loading paths of plastic related questions, in order to determine the subsequent damage cumulative rate under cyclic loading. Finally, the fatigue test of metal bolt connection is simulated numerically to verify the validity of the proposed model. Then, based on previous studies, a cumulative fatigue damage assessment method for metal bolt joints was proposed based on CDM theory and critical plane method [23]. A numerical approximation algorithm with fixed damage evolution rate based on periodic jump is used to avoid the calculation of cyclic stress history of total loading and unloading. Ahmadian et al. [24] studied the failure behavior of ceramic fiber-reinforced aluminum composites with initial holes under load by FE simulations. They find that pores significantly affect the mechanical strength of the composite. Gowayed et al. [25] studied the volume and direction of the defects in SiC/SiNC and MI-SiC /SiC composites utilized microscopic images. They investigated the effects of the defect volume fraction and orientation on the elastic properties of the materials. Xu et al. [26] established a FE model with random void defects to calculate the progressive damage in C/C braided composites under unidirectional stretching. It is found that void defect almost does not affect the elastic modulus and tensile strength of the C/C composite but significantly influences the failure behavior of the carbon matrix. Xu et al. [27] performed a nonlinear FE buckling analysis of the C/SiC composite plate and investigated the effect of initial defects particularly. In the framework of isometric analysis, Liu et al. [28] developed a formula for multilayer shells based on the layered deformation theory. Taking multilayer composite materials and sandwich plates as examples, the performance of the model was verified, and the accuracy of the proposed formula was verified by numerical results. Then, Liu et al. [29] a distributed plastic isometric frame model based on layer discretization is proposed to capture the plastic growth in a large deformation frame, and the effectiveness of the model is proved by an example of a beam yielding gradually under small deformation and large deformation. Recently, Liu et al. [30] developed a geometrically nonlinear continuous shell element for structural analysis of functionally graded materials, which can accurately describe the material properties of functionally graded materials varying with thickness. The performance of the equal-geometry continuous shell model is evaluated by some datum nonlinear shell problems, and the accuracy of the model is verified by numerical results.

The geometrical models should be established based on the actual structures for accurate numerical calculations for composite materials. Computed tomography (CT) technology has been widely used in medical and material science to get internal information about objects

[31, 32]. Huang et al. [33] used the threshold segmentation method to segment CT images of composites to construct the geometry mode. The same way was adopted in Zhu et al.'s work [34] to generate the FE models of aluminum foam. Many researchers have also established geometric models of braided composites based on CT images [35–40]. Sencu et al. [41] proposed a new fiber tracking algorithm that can effectively locate the fiber centerlines from CT images to generate the micro-scale FE models of composites. Mazars et al. [42] built a FE model of CMC material using CT images, which is used to calculate the damage of the composite in an in-situ tensile test. Gao et al. [43] studied 2D and 3D braided composites microstructure using synchrotron radiation X-ray microtomography. The cross-sections and 3D models are constructed, in which the pores are quantitatively analyzed. Ai SG et al. [44, 45] reconstructed the FE models of C/C and C/SiC composites based on CT images, in which the void defects were considered. Numerical simulations and material experiments have shown that the virtual material specimen which reveals internal defects had better calculation accuracy. Recently, Ge et al. [46] observed and reconstructed 3D braided composite geometry models using micro-CT scanning technology to investigate the effect of void defects on material strength and damage behavior. Yang et al. [47] reconstructed the internal structure of fabric-rubber composite using μ-CT scanning technology combined with deep learning neural network image processing and systematically studied its mechanical properties. The finite element method based on CT image develops rapidly, but there are still some problems and challenges. The reconstruction method of the fiber tows geometry model has been well developed, but the research of the matrix fidelity reconstruction method is less. The reason is that there are many irregular shape defects in the matrix, so it is very difficult to establish its geometric model. Most of the existing methods do not consider the defects in the matrix, establish a relatively ideal geometric model, or carry out statistical analysis of the defects in the matrix and then make them randomly distributed in the matrix model. At present, there have been some reports on the effect of defects on the damage and failure behavior of composite materials. However, the effect of actual defects on composite materials' damage and failure behavior is still not well understood.

In this paper, two groups of reconstruction models with different defect volume fractions (void volume fractions are 0, 1.52%, 3.04%, 4.56%, 6.08%, and 7.60%, respectively) and different defect geometry (wide hole, narrow hole, and elliptic hole with different aspect ratio) are established, respectively. The effects of defect volume fraction and defect geometry on damage behavior and tensile strength of C/SiC composites are studied and discussed. It is of great significance to further understand the influence of defects on the mechanical behavior of CMCs. In this study, μ-CT images of 2D plain-weave woven C/SiC composites are obtained by X-ray microtomography. The fiber tow and SiC matrix in the CT image is segmented by the threshold segmentation method and then filtered to reduce noise and enhance material boundaries, especially to retain the factual boundary information of defects in the matrix. A geometric model of C/SiC composites containing actual geometric defects is established for numerical simulation analysis based on the image segmentation results.

2 Materials and Method

2.1 Materials

The material studied in this paper is two-dimensional plain braided C/SiC composites prepared by isothermal Chemical-Vapor-Infiltrated (CVI) technology in Northwestern Polytechnical

University. The prefabricated parts (18 layers) were made of carbon fiber tows (T300,1 K) from Toray Corporation, Japan. Then 2D C/SiC laminates were prepared by the CVI method at 1000℃ for 240 h. The fiber volume fraction of C/SiC laminates was about 42%. To improve the properties of the fiber-matrix interface, pyro-carbon interphase was coated on the surface of carbon fiber with a thickness of about 2 μm before deposition of SiC matrix. Then a standard size sample is obtained by cutting (thickness: 4 mm).

2.2 Computed Tomography Test

A C/SiC composite specimen was scanned by an Xradia 510 Versa X-Ray Micro-Computed-Tomography system developed by Carl Zeiss. The beamline receives tunable X-rays in the energy range 30–160 keV with the maximum power of 10 W, and the spatial resolution is 0.7 μm. The CT images reported herein were collected using the X-rays of energy 60 keV 5 W to get the internal structural information of the materials. The scanning field is Φ 0.7 X 0.7 mm, and the voxel resolution is 2.0 μm. The total exposure period of the test was 7.2 h, with 994 CT images captured, as illustrated in Fig. 1b to c. The transmission images were collected and used to reconstruct the 3D images, which can be viewed by XM3DViewer. From the CT images, we can find that there are plenty of voids in the C/SiC specimen. More voids are located in the center of the specimen, and they are bigger than those near the surfaces.

2.3 Image-based FEM Method

2.3.1 CT Image Segmentation

As noted in Fig. 2a, there are four components in the virgin CT slices of the C/SiC composite: in-plane fiber tows (belt-like), out-of-plane fiber tows (oval-like), SiC matrix, and porosity defects. There are some challenges to segment the four components from
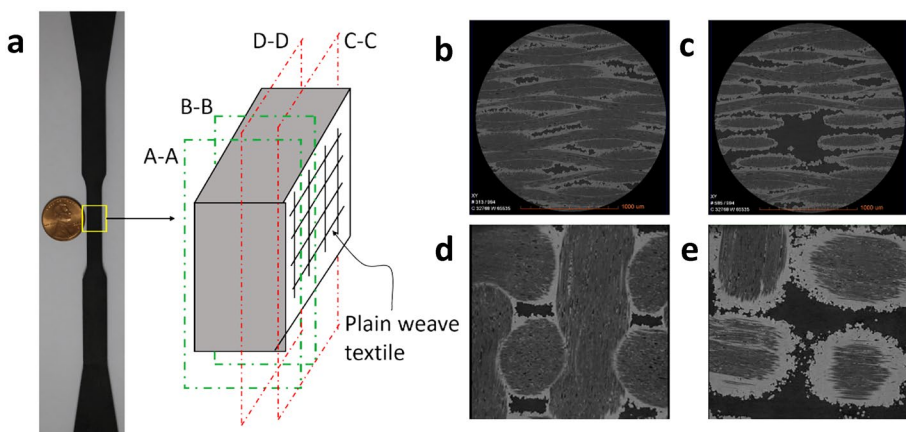

Fig. 1 CT images of C/SiC composite, **a** C/SiC sample and the CT slice locations, **b** CT image near the side surface of the specimen (section A-A), **c** CT image near the center of the specimen (section B-B), **d** CT image near the front surface of the sample (section C–C), (d) CT image near the center of the specimen (section D-D)
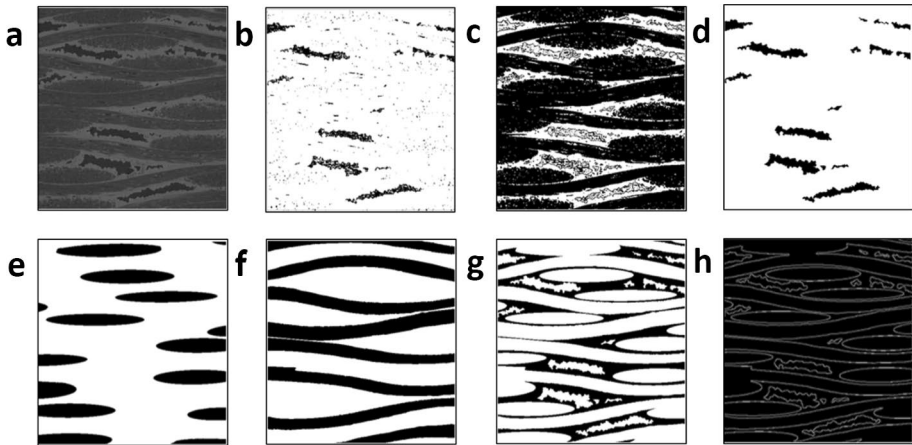
Fig. 2 CT image segmentation, **a** the virgin CT image of the C/SiC composite, **b** binary image of porosity defects, **c** binary image of fiber tows. **d** image of porosity defects after filtering, **e** image of out-of-plane fiber tows, **f** image of in-plane fiber tows, **g** image of SiC matrix, **h** boundaries of the four components in the C/SiC composite

the CT images because their gray levels are so close, especially for the in-plane and out-of-plane fiber tows.

This work adopted the threshold segmentation method to segment the CT images using the Matlab procedure. The threshold segmentation approach is a standard method to segment gray images, and the key for this method is how to select the threshold values. There are some methods to choose the threshold value, such as the Otsu method [22], iteration method, minimum error method, etc. For the CT images of the C/SiC composite, the gray distribution histogram has three peaks representing the three components in the composite: porosity defects, fiber tows, and SiC matrix. Therefore, the two gray values of the valleys were taken as the image segmentation thresholds (48 and 82) to segment the virgin CT images preliminarily, as presented in Fig. 2b and c.

The binary image of the porosity defects was obtained by the threshold segmentation method, whereas there is still a lot of noise in the picture, as illustrated in Fig. 2b. Some approaches reduce the noise, such as the corrosion and expansion method, median filtering, wavelet transform, etc. The actual shapes of defects and the SiC matrix will be somewhat affected when filtering the noise by those approaches. So in this work, a noise-detecting procedure based on the Matlab program was proposed to detect and filter the noise. First, a detection operator was created (the size of the detection operator is related to the size of the noise), which was used to detect the noise in the image. Then, by the coincidence degrees between the detection operator and the detection regions, it will be judged whether the detected area contains defects to reduce the influence of the noise filtering on the defect boundaries. It is observed in Fig. 2a, the cross-section shape of the out-of-plane fiber tows is approximately ellipse, so ellipse was adopted to fit the out-of-plane fiber tows, and the fitting results are plotted in Fig. 2e. By Boolean operation between Fig. 2c and e, noise filtering, and boundary smoothing, the in-plane fiber tows can be obtained, as shown in Fig. 2f. The SiC matrix can be obtained by Boolean operation, as noted in Fig. 2 (g), and the boundaries of the four components in the C/SiC composite are illustrated in Fig. 2h.

2.3.2 Image-based Finite Element Model

Firstly, we import these boundary images into the commercial software Auto CAD 2016 to generate 2D sketches, and then import the sketches into the 3D modeling software Pro/E for tensile modeling, and finally generate the 3D geometric model of C/SiC composites, as shown in Fig. 3a. Then the 3D geometric model was imported into Abaqus to generate the FE model of the C/SiC composite. The interactions between the fiber tows and SiC matrix were set as ideal adhesion (Tie). There are 164,868-node linear brick reduced integration elements (C3D8R) in the model in total.

We applied both in-plane stretching and out-plane stretching boundary conditions (Fig. 3a and b). For the boundary conditions of out-of-plane tension, we first apply displacement constraints in the X, Y, and Z directions and then applied displacement loads at the other end of the Z direction (0.62% of nominal strain). For the boundary conditions of in-plane tension, we first applied displacement constraints in the X, Y, and Z directions and then apply displacement loads on the other side of the X direction (0.67% of nominal strain). The components of the geometric model are shown in Fig. 3(c). In addition, in-plane and out-plane in this paper are defined relative to materials, not according to geometric models. In this paper, the out-of-plane direction refers to the Z direction of the model, and the in-plane direction refers to the X direction of the model, as shown in Fig. 3d.

This paper mainly studies the effect of the porosity defect fraction and geometric parameters on the mechanical properties of the C/SiC composite. To this end, two groups of virtual models were constructed. For group one, the models have different defect volume fractions ($V_d=0$, $V_d=1.52\%$, $V_d=3.04\%$, $V_d=4.56\%$, $V_d=6.08\%$ and $V_d=7.60\%$, some of the virtual models are illustrated in Fig. 4). For group two, models have different defect geometric parameters (wide defects, general defects, and narrow defects, as shown in Fig. 5). The defect geometry is the same for the virtual models in the first group but with different defect volume fractions. For the virtual models in the second group, the defect volume fraction is the same but with different defect geometric parameters.
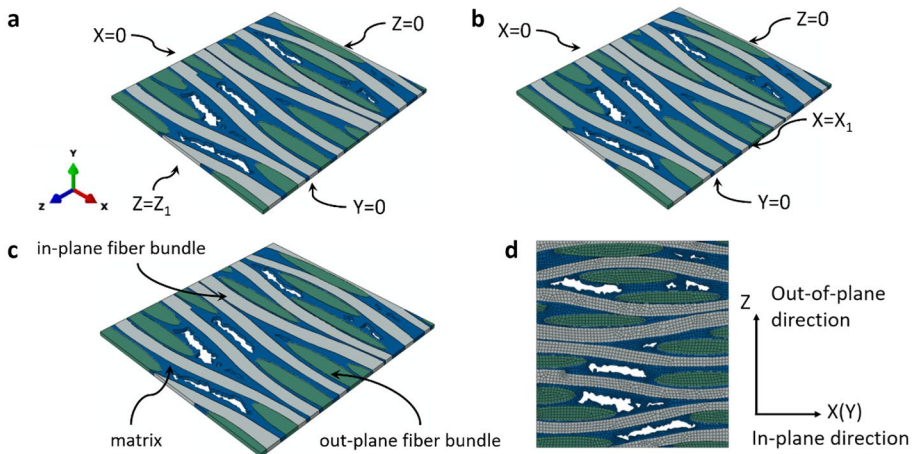

Fig. 3 **a b** The geometric model and boundary condition, **c** The geometric model component, **d** finite element mesh of the C/SiC composite
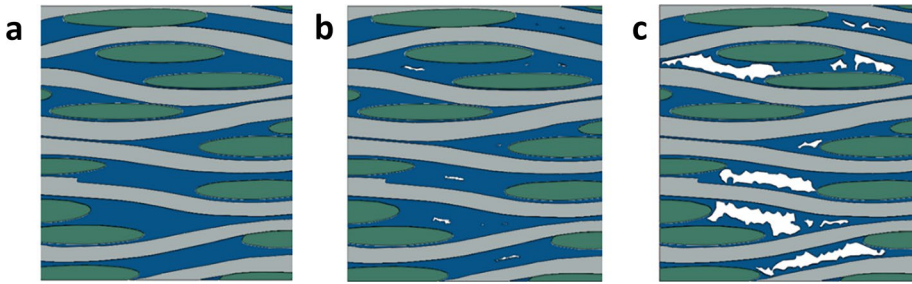
Fig. 4 Virtual models with different defect volume fractions **a** $V_d=0\%$, **b** $V_d=1.52\%$, **c** $V_d=7.60\%$

2.4 Progressive Damage Algorithm

The progressive damage criterion of the C/SiC composite used in the present study is a strain-based continuum damage formulation with different failure criteria applied to the SiC matrix and carbon fiber tows. The damage mechanism consists of two ingredients: the damage initiation criteria and the damage evolution law, which were detailed in our other work [44, 48].

Damage initiation and evolution criteria for the fiber tows in the longitudinal direction:

$$f_f^X = \sqrt{\frac{\varepsilon_{11}^{f,t}}{\varepsilon_{11}^{f,c}}\left(\varepsilon_{11}\right)^2 + \left[\varepsilon_{11}^{f,t} - \frac{\left(\varepsilon_{11}^{f,t}\right)^2}{\varepsilon_{11}^{f,c}}\right]\varepsilon_{11}} > \varepsilon_{11}^{f,t} \tag{1}$$

$$d_f^x = 1 - \frac{\varepsilon_{11}^{f,t}}{f_f^X}e^{\left(-C_{11}\varepsilon_{11}^{f,t}\left(f_f^X-\varepsilon_{11}^{f,t}\right)L^C/G_f\right)} \tag{2}$$

When the damage satisfies the damage initiation criterion (1), damage evolution will be carried out according to the evolution criterion (2). L^C is the characteristic length associated with the material point. $\varepsilon_{11}^{f,t}$ and $\varepsilon_{11}^{f,c}$ are the tensile failure strain and compression failure strain of the fiber tow, respectively. C_{ij} represents the component of the elastic matrix in the undamaged state.
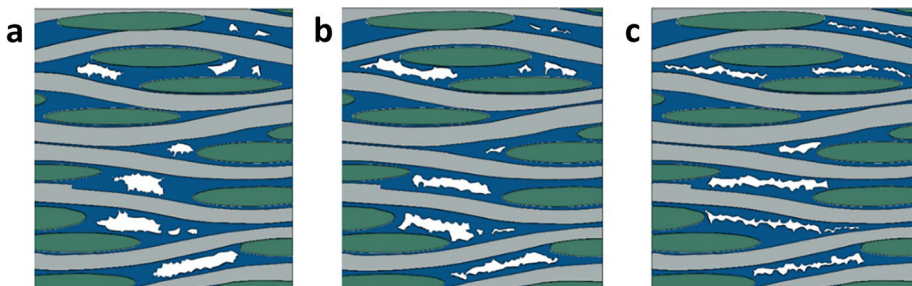

Fig. 5 Virtual models with **a** wide defects, **b** general defects, and **c** narrow defects

Damage initiation and evolution criteria for the fiber tows in the transverse direction:

$$f_m^Y = \sqrt{\frac{\varepsilon_{22}^{f,t}}{\varepsilon_{22}^{f,c}}\left(\varepsilon_{22}\right)^2 + \left[\varepsilon_{22}^{f,t} - \frac{\left(\varepsilon_{22}^{f,t}\right)^2}{\varepsilon_{22}^{f,c}}\right]\varepsilon_{22} + \left(\frac{\varepsilon_{22}^{f,t}}{\varepsilon_{12}^{f,s}}\right)^2\left(\varepsilon_{12}\right)^2} > \varepsilon_{22}^{f,t} \tag{3}$$

$$d_m^Y = 1 - \frac{\varepsilon_{22}^{f,t}}{f_m^Y}e^{\left(-C_{22}\varepsilon_{22}^{f,t}\left(f_m^Y - \varepsilon_{22}^{f,t}\right)L^C/G_m\right)} \tag{4}$$

Equation (3) is the damage initiation criterion for the fiber tows in the transverse direction. Evolution is carried out when the damage satisfies the damage initiation criterion (3), evolution is carried out according to (4). Where $\varepsilon_{22}^{f,t}$ and $\varepsilon_{22}^{f,c}$ are the failure strains of the fiber tow during stretching and compression in the in-plane direction, and the $\varepsilon_{12}^{f,s}$ is shear failure strain in the 1 and 2 directions. The effective elasticity matrix of the fiber tow is related to three damage variables, d_f^x, d_m^Y and d_m^Z, which is given by

$$C_d^f = \begin{bmatrix} \left(1-d_f^X\right)C_{11} & \left(1-d_f^X\right)\left(1-d_m^Y\right)C_{12} & \left(1-d_f^X\right)\left(1-d_m^Z\right)C_{13} & & & \\ & \left(1-d_m^Y\right)C_{22} & \left(1-d_m^Y\right)\left(1-d_m^Z\right)C_{23} & & \textit{Zero} & \\ & & \left(1-d_m^Z\right)C_{33} & & & \\ & & & \left(1-d_f^x\right)\left(1-d_m^Y\right)C_{44} & & \\ & \textit{Symmetric} & & & \left(1-d_f^X\right)\left(1-d_m^Z\right)C_{55} & \\ & & & & & \left(1-d_m^Y\right)\left(1-d_m^Z\right)C_{66} \end{bmatrix} \tag{5}$$

Fiber tows are in the X(1)-Y(2)-Z(3) Cartesian coordinate system, and the Z direction corresponds to the fiber longitudinal direction. Using a user-defined subroutine UMAT, the progressive damage and failure of the C/SiC composite are investigated. Three damage variables, SDV1, SDV2, and SDV3, are used to indicate damages for fiber tows in transverse (*T* and *Z*) and longitudinal (*L*) directions, respectively. Also, three damage variables, SDV1, SDV2, and SDV3, indicate damages for the SiC matrix in X, Y, and Z directions, respectively [44, 48]. When SDV1 = 0, the material is intact, SDV1 = 1, the material is damaged (with no load capacity). The carbon fiber tow is a transverse anisotropic material, and the SiC matrix is isotropic material.

The material parameters used in the numerical simulation in this paper are listed in Table 1. Both the SiC matrix and carbon fibers were treated as elastic materials. The mechanical parameters of the carbon fibers are listed in Table 1. The mechanical parameters (E_{f11}, G_{f12}, G_{f23}, υ_{f12}, υ_{f23}) of the carbon fiber tows in the three orthogonal directions (1, 2, 3) can be calculated using the properties of the component materials (fiber and matrix), and the micromechanics formulae have been given in Ref. [49].

Where V_c is the volume fraction of the carbon fiber and $V_c = 0.685$ in this study, E_{f11}, E_{f22} is Young's elastic modulus of the carbon fiber in longitudinal and transverse directions, respectively. G_{f12}, G_{f23} is the shear modulus of the carbon fiber in 1–2 and 2–3 planes, respectively. Also, υ_{f12} is the Poisson's ratio of the carbon fiber. E_m, υ_m and G_m represent Young's elastic modulus, Poisson's ratio, and shear modulus of the SiC matrix, respectively.

Table 1 Mechanical property parameters

	E_{11} (GPa)	E_{22} (GPa)	ν_{12}	G_{12} (GPa)	G_{23} (GPa)	X_{T11} (MPa)	X_{C11} (MPa)	S (MPa)	G (N/m)
Carbon fiber	230 [50]	40 [51]	0.26 [51]	24 [51]	14.3 [51]	2107 [49]	-	-	5.0 [52]
SiC matrix 1	93.37 [45]	-	0.21 [45]	-	-	104.3 [53]	-	46.2 [54]	0.5 [45]
SiC matrix 2	193.78	-	0.21	-	-	207.6 [53]	-	88.2 [54]	1.0
Fiber tow	188.15	44.52	0.26	26.82	16.48	$X_{T11}=1268.3$ $X_{T22}=78.9$	1141.5	$S_{12}=28.2$	$G_f=3.6$ [45] $G_m=0.5$ [45]

SiC matrix 1 is the SiC matrix insider the fiber tows, and SiC matrix 2 is the SiC matrix outsider the fiber tows. G is the fracture energy

$$\begin{cases} E_{11} = V_c E_{f11} + (1 - V_c)E_m \\[2mm] E_{22} = E_{33} = \dfrac{E_m}{1 - \sqrt{V_c} \times (1 - E_m/E_{f22})} \\[3mm] G_{12} = G_{13} = \dfrac{G_m}{1 - \sqrt{V_c}(1 - G_m/G_{f12})} \\[3mm] G_{23} = \dfrac{G_m}{1 - \sqrt{V_c}(1 - G_m/G_{f23})} \\[3mm] v_{12} = v_{13} = V_c v_{f12} + (1 - V_c)v_m \\[2mm] v_{23} = E_{22}/(2G_{23}) - 1 \end{cases} \tag{6}$$

3 Results and Discussions

The quasi-static tensile tests of C/SiC composites were repeated three times. The samples used are shown in Fig. 6a. The tensile testing machine used is shown in Fig. 6b. A quasi-static displacement control loading (0.5 mm/min) was used to obtain the stress–strain curve during the experiment. Experimental results are shown in Fig. 6c. The experimental results show that the strength of the C/SiC composite is 304.20 MPa. The model with 6.08% defect volume fractions in this paper was established based on the actual defect geometry and defect volume fraction in real materials (other models studying the effect of defect volume fraction on mechanical properties of materials have the same defect geometry and different defect volume fractions. This better reflects the impact of the geometry of the defect.), and the strength obtained by numerical calculation was 325.86 MPa. The error is about 7.12%.
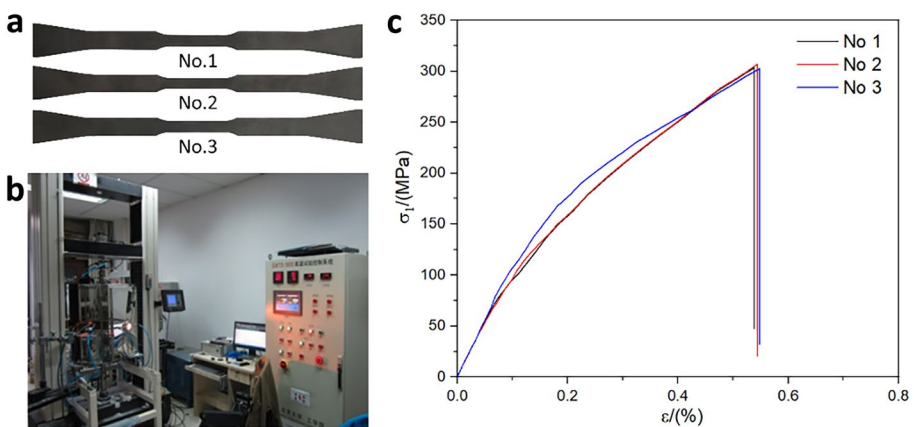

Fig. 6 **a** C/SiC test specimens, **b** tensile testing machine, **c** stress–strain curve of C/SiC tensile test

3.1 The Influence of Void Defect Fraction

3.1.1 In-plane Tension

The failure process and tensile strengths of the C/SiC composite with different void defect fractions are obtained, and the failure features of the fiber tows and SiC matrix are illustrated in Fig. 7. The simulation results show that the initial damage location in the fiber tows is the same. In contrast, the final failure features of the fiber tows are greatly affected by the void defects, as plotted in Fig. 7.

Figures 7 (a) and (b) (ε=0.67%) illustrate the failure features of the fiber tows. In the virtual model V_d=6.08%, the material damage is located in the second, third, and fifth fiber tows. In this virtual model, void defects are located near the second, third, fourth, and fifth tows damaged sites. It indicates that the void defects greatly influence the damage and failure of the fiber tows. With the increase of the defect volume fraction, the damage in the SiC matrix becomes more and more serious, and the material damage mainly occurs around the defect. This phenomenon is more evident in the virtual models with void defect volume fractions larger than 1.52%. The material damage propagation in the SiC matrix in each virtual model is also different. The higher the defect volume fraction, the more pronounced the damage propagation. It should be noted that the SiC matrix may also damage at other locations and result in the degradation of the carrying capacity of the materials that have not yet failed. It is more likely to occur in the SiC matrix in the virtual models with larger defect fractions, which indicates that the void defects can result in the earlier failure of the SiC matrix surrounding these voids and reduce the load-bearing properties of the matrix.

Figure 8 plots the equivalent tensile stress–strain curves of the C/SiC virtual models with different defect volume fractions. The pattern of the stress–strain curves is the same. Before the stress reaches the peak value, material damage mainly occurs in the SiC-matrix, slightly fluctuating the equivalent stress–strain curves. When the stress reaches the peak value, material damage occurs in fiber tows and affects the loading capacity of the C/SiC composite. However, this effect is different from that result by the damage of the
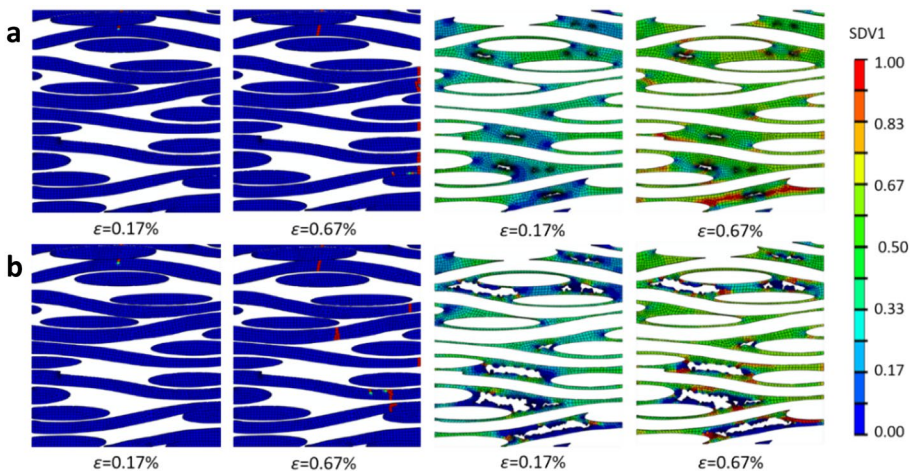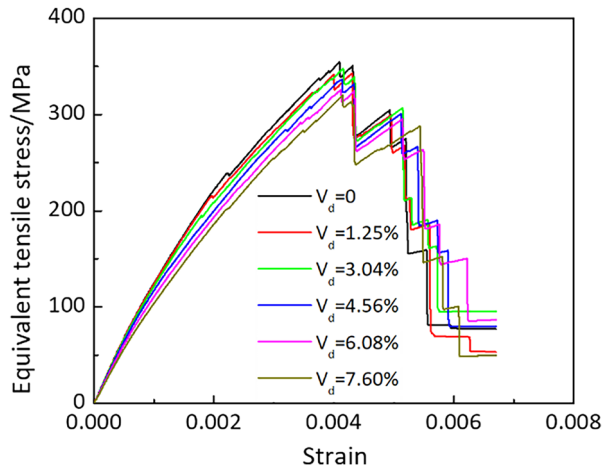

Fig. 7 The damage evolution in fiber tows and CVI-SiC matrix **a** V_d=1.52%. **b** V_d=6.08%

Fig. 8 Equivalent tensile stress–strain curves of C/SiC virtual models with different defect volume fractions under in-plane unidirectional tension

SiC-matrix. The deterioration of fiber tows would induce the failure of the whole fiber tows in a short time. The sharp drops in the stress–strain curves indicate the fracture of fiber tows. It should be noted out that the number of stress drops in a stress–strain curve is not exactly consistent with the total number of fiber tows, as there are multiple fiber tows broke simultaneously. Figure 8 indicates that with the increment of void defect volume fraction, the tensile strength of the C/SiC virtual models gradually decreases. The tensile strength difference between the model $V_d=0$ and the model $V_d=7.60\%$ is 34.46 MPa ($\approx$9.7%). In addition, the time of fiber tow damage is almost the same in all models.

3.1.2 Out-of-plane Tension

Figure 9 illustrated the damage evolution in the fiber tows and SiC matrix, taking the virtual models $V_d=1.52\%$ and $V_d=6.08\%$ as examples. It is clear that, under the out-of-plane
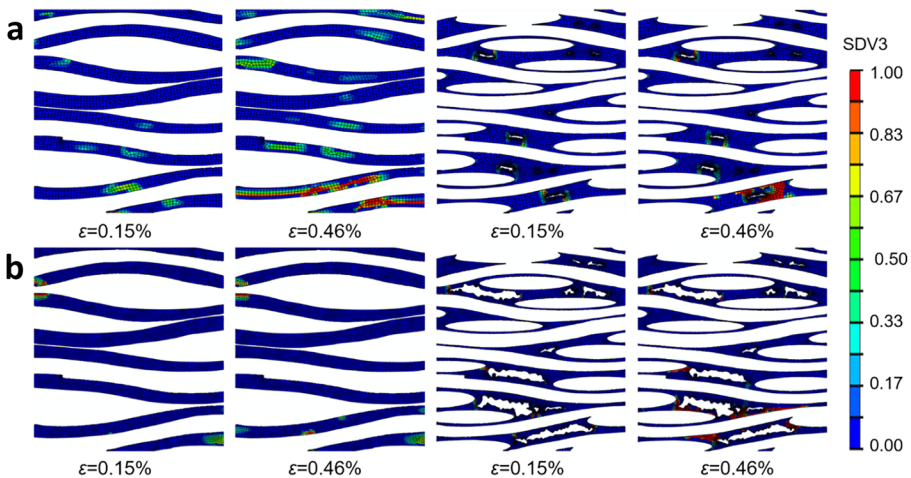

Fig. 9 The damage evolution in fiber tows and CVI-SiC matrix **a** $V_d=1.52\%$, **b** $V_d=6.08\%$

tension, material damage mainly occurs in the SiC matrix. Material damage in the fiber tows is only found in some fiber tows in the virtual model with low defect fractions. The fiber tows are transversal tensile damaged (SDV 3), as presented in Fig. 9a. The material damage in fiber tows decreases with defect volume fraction increasing, as plotted in Fig. 9. The SiC matrix has serious damage around void defects, especially in the big-sized voids matrix. With the increase of tensile load, material damage gradually extends from the defect boundary to the fiber tow. It then continues to expand along with the interface between the fiber tow and SiC matrix until the failure of the model (transverse failure or damage of the fiber tow extends along with the interface between the fiber tow and SiC matrix to the model boundary). This phenomenon usually occurs where defects are concentrated. In the process of damage propagation, these defects are more likely to form a connection phenomenon, resulting in earlier extension of damage to the interface between fiber tow and matrix and further expansion, and even lead to fiber tow damage.

Most fiber tows almost didn't damage and fracture under the out-of-plane tension, so there is no step-like drop for the stress–strain curves, as illustrated in Fig. 10. However, the defect has a significant effect on the out-of-plane tensile strength of the C/SiC composite. With the defect volume fraction increasing, the out-of-plane tensile strength decreased. The out-of-plane tensile strength of the virtual model $V_f=0$ is 65.43 MPa, while the virtual model $V_f=7.60\%$ is 23.65 MPa, which decreased by 63.85%. Except that the strength decreased by 3.0% between $V_d=0$ and $V_d=1.25\%$, the strength of the other models decreased by 21.8%, with the defect volume fraction increasing gradually.

3.2 The Influence of Defect Geometry

3.2.1 In-plane Tension

Progressive damage features of the three C/SiC virtual samples with different defect geometries, as illustrated in Fig. 11, under in-plane tension, are numerically studied. The failure process and in-plane tensile strengths at room temperature of the five samples have been obtained. From the simulation results, it can be seen that the initial damage features of the fiber tows are the same. The final fiber tow and matrix damage of the two virtual models

Fig. 10 Equivalent tensile stress–strain curves of C/SiC virtual models with different defect volume fractions under out-of-plane tension
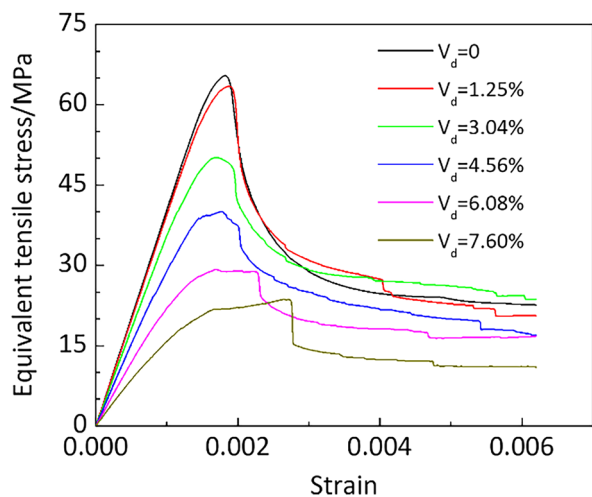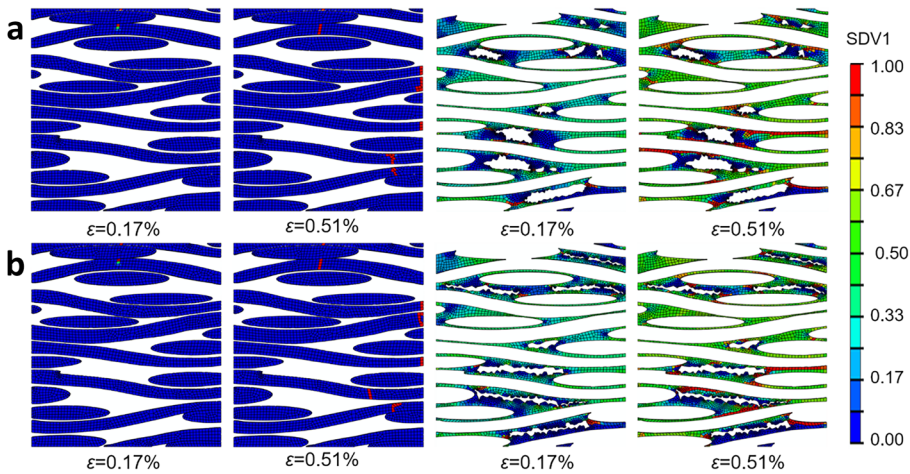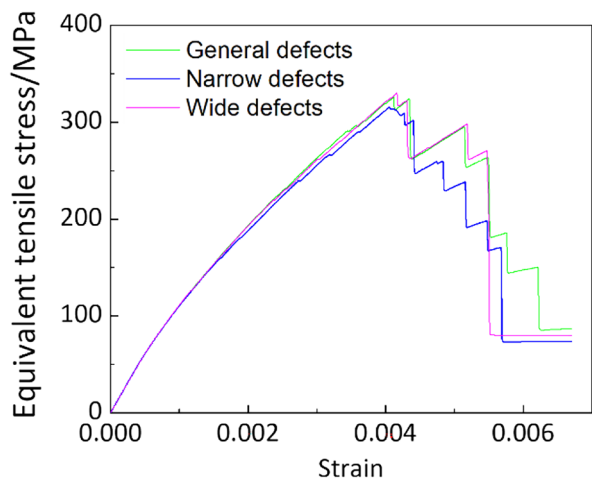
Fig. 11 Material damage in fiber tows and SiC matrix for the virtual models with **a** wide defects and **b** narrow defects under in-plane tension

with wide defects and narrow defects are shown in Fig. 11. As shown in Fig. 11a and b, the damage of the fiber tow as a whole is basically the same in the two models with wider and narrower defects, indicating that the geometric characteristics of the defect have little influence on the damage location of the fiber tow. From the simulation results, the initial damage in the SiC matrix mainly occurs around the defects, especially at both ends of the defects in the length direction. With the tensile load increases, the damage evolution in the SiC matrix in the three virtual models is different. The matrix around a wide defect is more likely to be damaged and expanded in a narrow position, while the matrix around a narrow defect is more likely to be damaged at both the ends of a defect in the length direction.

Figure 12 shows the stress–strain curves of the three C/SiC virtual models with different defect geometries. In general, the stress–strain curves of the three models are similar in shape but different after the second decline of the curves. Before material damage

Fig. 12 Equivalent in-plane tensile stress–strain curves of the C/SiC virtual models with different defect geometries
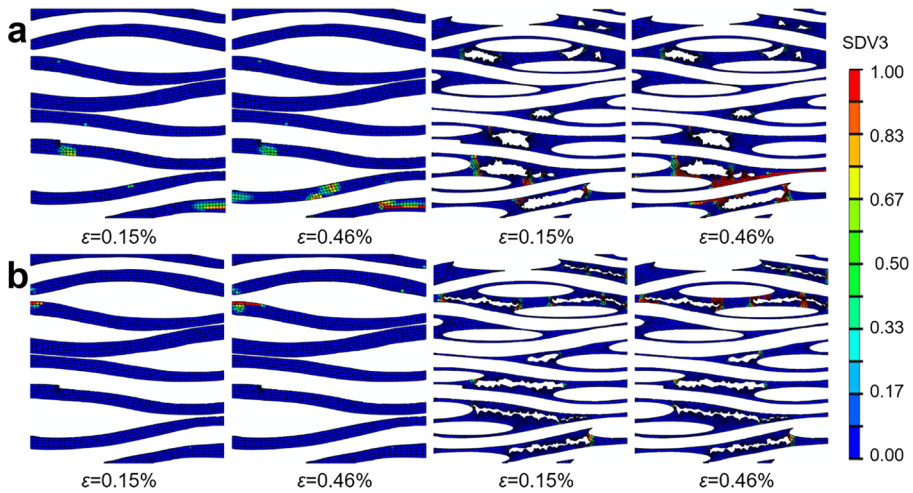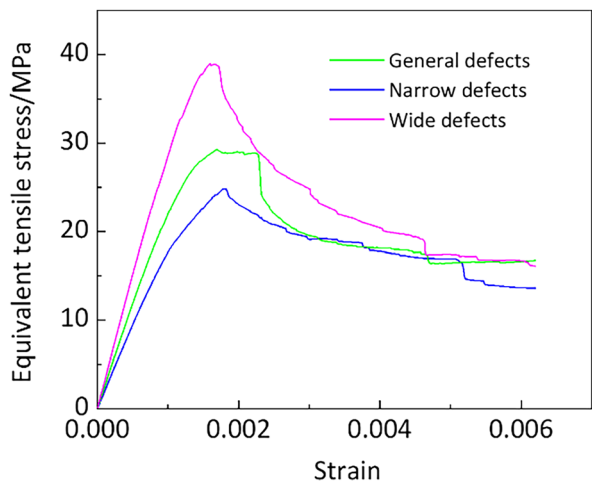
Fig. 13 Material damage in fiber tows and SiC matrix for the virtual models with **a** wide defects and **b** narrow defects under out-of-plane tension

occurred in the model (about $\varepsilon < 0.15\%$), the equivalent tensile stress–strain curves were almost coincident. The in-plane tensile strength of the virtual model with narrower defects is lower than the strengths of the other two models, while the strength of the virtual model with wider defects is the highest. It indicates that narrow defects are more likely to cause material damage and failure of the C/SiC composites, while wide defects have less influence on the in-plane tensile strength of the C/SiC composites.

3.2.2 Out-of-plane Tension

Progressive damage features of the three C/SiC virtual samples with different defect geometries under out-of-plane tension were numerically studied, as illustrated in Fig. 13. Under

Fig. 14 Equivalent out-of-plane tensile stress–strain curves of the C/SiC virtual models with different defect geometries

the out-of-plane tensile load, material damage in the fiber tows for the three C/SiC virtual models is slight. Material damage in the SiC matrix does not appear and expand around all defects, but most of them only appear in the positions where defects are denser. It then expands along with the interface between the fiber tow and SiC matrix, causing the fiber tow to fail or expand to the model boundary, as shown in Fig. 13.

The out-of-plane equivalent tensile stress–strain curves of the three C/SiC virtual models with different defect geometries are plotted in Fig. 14. The strength of the virtual model with wide defects is significantly higher than the strengths of the other two virtual models. It indicates that longer defects are more likely to cause the C/SiC composite failure under the out-of-plane tensile load. As shown in Fig. 14, the virtual model with narrow defects has the lowest strength (24.86 MPa), while the model with wide defects has the highest strength (38.96 MPa), with a difference of 56.7%. Besides, the three stress–strain curves have different shapes, and it indicates that the defect geometry has a significant influence on the failure process of the C/SiC composites.

4 Conclusions

In this paper, μ-CT images are used to establish the image-based FE models of a plain-woven C/SiC composite. Based on the IB-FEM approach, numerical simulations are carried out to investigate the influences of matrix void defects on the mechanical properties of the C/SiC composite. The results show that the out-of-plane tensile strength is more sensitive to the volume fraction of void defects. When the void volume fraction increases by 1%, the tensile strength decreases by 14.34%. The in-plane tensile strength difference between the model V = 0 and the model V = 7.60% is about 9.7%. Under in-plane tension, the damage appears around every void and extends along with the interface between the fiber tow and the matrix, eventually leading to fiber tow fracture. However, under the out-plane tension, the material damage appears around some concentrated voids. It then expands along with the interface between the fiber tow and the matrix, failing the fiber tow and the whole model. The numerical results also show that the tensile strength of the C/SiC composite is more sensitive to the narrow void defects, especially for the out-plane tensile strength. Specifically summarized as the following conclusions:

(1) Under in-plane tension, material damage initially occurs in the SiC matrix surrounding the defects, and this phenomenon becomes more serious with the defect volume fraction increase. When the load reaches the peak value, the fiber bundles break suddenly, which triggers the fracture of the composites. The in-plane tensile strength of the C/SiC composite decreases slightly with the increase of defect volume fraction.

(2) Under out-of-plane tension, material damage occurs in the SiC matrix around the defects. It expands along with the SiC matrix-fiber bundles interfaces, eventually result in the failure of the C/SiC composite. The out-of-plane tensile strength decreases sharply with the increase of defect volume fraction.

(3) Defect geometry has little effect on the in-plane tensile strength of the C/SiC composites but has a significant impact on the out-of-plane tensile strength of the C/SiC composites. The virtual model with narrow defects has the minimum tensile strength of the C/SiC composites, both the in-plane and out-of-plane tensile strength.

Data Availability We statement that all data related to this article will be made available at reasonable request.

References

1. Du, J.G., Zhang, H.Z., Geng, Y.M., Ming, W.Y., He, W.B., Ma, J., Cao, Y., Li, X.K., Liu, K.: A review on machining of carbon fiber reinforced ceramic matrix composites. Ceram. Int. **45**, 18155–18166 (2019)
2. Wang, X.L., Gao, X.D., Zhang, Z.H., Cheng, L.S., Ma, H.P., Yang, W.M.: Advances in modifications and high-temperature applications of silicon carbide ceramic matrix composites in aerospace: A focused review. J. Eur. Ceram. Soc. **41**(9), 4671–4688 (2021)
3. Su, F., Huang, P.F.: Microscopic Mechanism of the High-Temperature Strength Behaviour of a C/SiC Composite. Appl. Compos. Mater. **26**, 1059–1071 (2019)
4. Naresh K., Khan K.A., Umer R., Cantwell W.J.: The use of X-ray computed tomography for design and process modeling of aerospace composites: A review Mater. Des. **190**, 108533 (2020)
5. Galizia, P., Zoli, L., Sciti, D.: Impact of residual stress on thermal damage accumulation, and Young's modulus of fiber-reinforced ultra-high temperature ceramics. Mater. Des. **160**, 803–809 (2018)
6. Meyer, P., Waas, A.M.: FEM predictions of damage in continous fiber ceramic matrix composites under transverse tension using the crack band method. Acta Mater. **102**, 292–303 (2016)
7. Zhang, S., Gao, X.G., Song, Y.D.: In Situ Strength Model for Continuous Fibers and Multi-Scale Modeling the Fracture of C/SiC Composites. Appl. Compos. Mater. **26**, 357–370 (2019)
8. Ai, S.G., Fu, H.L., He, R.J., Pei, Y.M.: Multi-scale modeling of thermal expansion coefficients of C/C composites at high temperature. Mater. Des. **82**, 181–188 (2015)
9. Chen, X.H., Sun, Z.G., Chen, P., Song, Y.D., Niu, X.M.: Modeling Thermal Expansion Behavior of 2.5 D C/SiC Composites in Air Oxidizing Environments between 400 °C and 800 °C. Appl. Compos. Mater. **27**, 861–875 (2020)
10. Zhao, Y.N., Chen, Y.F., He, C.W., Ai, S.G., Fang, D.N.: A damage-induced short-circuit diffusion model applied to the oxidation calculation of ceramic matrix composites (CMCs) Compos. A: Appl. Sci. Manuf. **127**, 105621 (2019)
11. Gao, X.G., Han, X., Song, Y.D.: X-ray computed tomography based microstructure reconstruction and numerical estimation of thermal conductivity of 2.5D ceramic matrix composite. Ceram.Int. **43**, 9790–9797(2017)
12. Daggumati, S., Sharma, A., Kasera, A., Upadhyay, N.: Failure Analysis of Unidirectional Ceramic Matrix Composite Lamina and Cross-Ply Laminate under Fiber Direction Uniaxial Tensile Load: Cohesive Zone Modeling and Brittle Fracture Mechanics Approach. J. of Materi Eng and Perform **29**, 2049–2060 (2020)
13. Chen, X.H., Sun, Z.G., Sun, J.F., Song, Y.D.: Simulation of Degraded Properties of 2D plain Woven C/ SiC Composites under Preloading Oxidation Atmosphere. Appl. Compos. Mater. **24**, 1287–1307 (2017)
14. Wang, F.Y., Cheng, L.F., Liang, S.H.: Effects of Pore on Thermal Diffusivity and Thermal Radiation Properties of C/SiC Composites at High Temperatures. Appl. Compos. Mater. **26**, 1411–1422 (2019)
15. Chen, Y.F., Zhao, Y.N., Ai, S.G., He, C.W., Tao, Y., Yang, Y.Z., Fang, D.N.: A constitutive model for elastoplastic-damage coupling effect of unidirectional fiber-reinforced polymer matrix composites. Compos. A: Appl. Sci. Manuf. **130**, 105736 (2020)
16. Kumar, R.S.: Effects of randomly distributed defects on Mode-I interlaminar fracture of composite materials. Eng Fract Mech. **248**, 107699 (2021)
17. Hausherr, J.M., Wagner, L., Gorywod, M.: Fabrication of artificial defects and their effect on the mechanical properties of C/C-SiC. J. Eur. Ceram. Soc. **40**, 636–641 (2020)
18. Dong, H.N., Gao, X.G., Song, Y.D.: Prediction model of matrix crack density in ceramic matrix composites under arbitrary matrix stress distribution. Mech. Adv. Mater. Struc. (2020)
19. Xiao, J., Liu, N., Lua, J., Saathoff, C., Seneviratne, W.: Data-Driven and Reduced-Order Modeling of Composite Drilling. AIAA SciTech Forum. 1859 (2020)
20. Liu, N., Jeffers, A.E.: Rational Bézier triangles for the analysis of is geometric higher-order gradient damage models, in: 13th World Congress on Computational Mechanics (WCCM XIII) and 2nd

Pan American Congress on Computational Mechanics (PANACM II), New York City, NY, USA, July 22–27, (2018)

21. Liu, N., Jeffers, A.E.: Feature-preserving rational Bézier triangles for isogeometric analysis of higher-order gradient damage models. Comput. Methods Appl. Mech. Engrg. **357**, 112585 (2019)

22. Liu, N., Xiao, J., Cui, X.D., Liu, P., Lua, J.: A Continuum Damage Mechanics (CDM) Modeling Approach for Prediction of Fatigue Failure of Metallic Bolted Joints. AIAA SciTech Forum. 0237 (2019)

23. Liu, N., Cui, X.D., Xiao, J., Lua, J., Phan, N.: A simplified continuum damage mechanics based modeling strategy for cumulative fatigue damage assessment of metallic bolted joints. Int. J. Fatigue. **131** 105302 ,(2020)

24. Ahmadian, H., Liang, B., Soghrati, S.: Analyzing the impact of microstructural defects on the failure response of ceramic fiber reinforced aluminum composites. Int. J. Solids. Struc. **97–98**, 43–55 (2016)

25. Gowayed, Y., Ojard, G., Prevost, E., Santhosh, U., Jefferson, G.: Defects in ceramic matrix composites and their impact on elastic properties. Compos. B: Eng. **55**, 167–175 (2013)

26. Xu, J., Lu, X.F., Zhu, X.L.: Effect of Random Void Defects on the Mechanical Behavior of C/C Braided Composites. Adv. Eng. Mater. **20**, 1701164 (2018)

27. Xu, Y.J., Ren, S.X., Zhang, W.L., Wu, Z.Q., Gong, W.R., Li, H.B.: Study of thermal buckling behavior of plain woven C/SiC composite plate using digital image correlation technique and finite element simulation. Thin Wall Struct. **131**, 385–392 (2018)

28. Liu, N., Jeffers, A.E.: Isogeometric analysis of laminated composite and functionally graded sandwich plates based on a layerwise displacement theory. Compos. Struct. **176**, 143–153 (2017)

29. Liu, N., Jeffers, A.E.: Adaptive isogeometric analysis in structural frames using a layer-based discretization to model spread of plasticity. Comput Struct. **196**, 1–11 (2018)

30. Liu, N., Ren, X., Lua, J.: An isogeometric continuum shell element for modeling the nonlinear response of functionally graded material structures. Compos. Struct. **237**, 111893 (2020)

31. Wang, L., Zhang, W., Li, H.B., Hou, C.T., Ren, F.: 3D In-Situ Characterizations of Damage Evolution in C/SiC Composite under Monotonic Tensile Loading by Using X-Ray Computed Tomography. Appl. Compos. Mater. **27**, 119–130 (2020)

32. Wang, F., Pirzada, T.J., Liu, R.J., Wang, Y.F., Zhang, C.R., Marrow, T.J.: Microstructure Characterization by X-Ray Computed Tomography of C/C-SiC Ceramic Composites Fabricated with Different Carbon Fiber Architectures. Appl. Compos. Mater. **26**, 1247–1260 (2019)

33. Huang, W.K., Zhang, X.N., Yin, Y.M.: An Image-Based Finite Element Approach for Simulating Viscoelastic Response of Asphalt Mixture. Adv. Mater. Sci. Eng. 7428623 (2016)

34. Zhu, X.L., Ai, S.G., Fang, D.N., Liu, B., Lu, X.F.: A novel modeling approach of aluminum foam based on MATLAB image processing. Comp. Mater. Sci. **82**, 451–456 (2014)

35. Rossol, M.N., Fast, T., Marshall, D.B., Cox, B.N., Zok, F.W.: Characterizing In-Plane Geometrical Variability in Textile Ceramic Composites. J. Am. Ceram. Soc. **98**, 205–213 (2015)

36. Li, Y., Hao, J., Wang, Z.G., Guan, Z.Z., Liu, J.L., Jin, C.Y.: Influence of ultra-high-rise pumping on microstructure and multi-scale mechanical properties of concrete based on X-ray CT and 3D mesoscopic numerical simulation. Constr Build Mater. **267**, 120980 (2021)

37. Rinaldi, R.G., Blacklock, M., Bale, H., Begley, M.R., Cox, B.N.: Generating virtual textile composite specimens using statistical data from micro-computed tomography: 3D tow representations. J. Mech. Phys. Solids. **60**, 451–470 (2012)

38. Bale, H., Blacklock, M., Begley, M.R., Marshall, D.B., Cox, B.N., Ritchie, R.O.: Characterizing three-dimensional textile ceramic composites using synchrotron x-ray micro-computed-tomography. J. Am. Ceram. Soc. **95**, 392–402 (2012)

39. Blacklock, M., Shaw, J.H., Zok, F.W., Cox, B.N.: Virtual specimens for analyzing strain distributions in textile ceramic composites. Compos. A: Appl. Sci. Manuf. **85**, 40–51 (2016)

40. Ghaedsharaf, M., Brunel, J.E., Lebel, L.L.: Fiber-level numerical simulation of biaxial braids for mesoscopic morphology prediction validated by X-ray computed tomography scan. Compos. B. Eng. **218**, 108938 (2021)

41. Sencu, R.M., Yang, Z., Wang, Y.C., Withers, P.J., Rau, C., Parson, A., Soutis, C.: Generation of micro-scale finite element models from synchrotron X-ray CT images for multidirectional carbon fibre reinforced composites. Compos. A: Appl. Sci. Manuf. **91**, 85–95 (2016)

42. Mazars, V., Caty, O., Couégnat, G., Bouterf, A., Roux, S., Denneulin, S., Pailhès, J., Vignoles, C.L.: Damage investigation and modeling of 3D woven ceramic matrix composites from X-ray tomography in-situ tensile tests. Acta Mater. **140**, 130–139 (2017)

43. Gao, Y.T., Wang, Y.D., Yang, X.M., Liu, M., Huai, P., Zhou, X.T.: Synchrotron X-ray tomographic characterization of CVI engineered 2D-woven and 3D-braided SiC$_f$/SiC composites. Ceram. Int. **42**, 17137–21714 (2016)

44. Ai, S.G., Fang, D.N., He, R.J., Pei, Y.M.: Effect of manufacturing defects on mechanical properties and failure features of 3D orthogonal woven C/C composites. Compos. B: Eng. **71**, 113–121 (2015)
45. Ai, S.G., Song, W.L., Chen, Y.F.: Stress field and damage evolution in C/SiC woven composites: Image-based finite element analysis and in situ X-ray computed tomography tests. J. Eur. Ceram. Soc. **41**, 2323–2334 (2021)
46. Ge, L., Li, H.M., Zhong, J.H., Zhang, C., Fang, D.N.: Micro-CT based trans-scale damage analysis of 3D braided composites with pore defects. Compos Sci Technol. **211**, 108830 (2021)
47. Yang, H., Wang, W.F., Shang, J.C., Wang, P.D., Lei, H.S., Chen, H.S., Fang D.N.: Segmentation of computed tomography images and high-precision reconstruction of rubber composite structure based on deep learning. Compos Sci Technol. **213**, 108875 (2021)
48. Linde, P., Pleitner, J., Boer, H.D., Carmone, C.: Modelling and Simulation of Fibre Metal Laminates. In ABAQUS Users Conference. (2004)
49. Christos, C.C.: Mechanics of composite materials: past, present, and future. NASA technical memorandum 100793, in 21st Annual Meeting of the Society for Engineering Science, Blacksburg, Virginia, October 15–17 (1984)
50. Sauder, C., Lamon, J., Pailler, R.: Thermomechanical properties of carbon fibres at high temperatures (up to 2000 °C). Compos. Sci. Technol. **62**, 499–504 (2002)
51. Fang, G.D., Liang, L., Wang, B.L.: Progressive damage and nonlinear analysis of 3D four-directional braided composites under unidirectional tension. Compos. Struct. **89**, 126–133 (2009)
52. ABAQUS 6.13 User's Manual. ABAQUS Inc, 2013; Pawtucket, RI, USA
53. Snead, L.L., Nozawa, T., Katoh, Y., Byun, T.S., Kondo, S., Petti, D.A.: Handbook of SiC properties for fuel performance modeling. J. Nucl. Mater. **371**, 329–377 (2007)
54. Cockeram, B.V.: Flexural Strength and Shear Strength of Silicon Carbide to Silicon Carbide Joints Fabricated by a Molybdenum Diffusion Bonding Technique. J. Am. Ceram. Soc. **88**, 1892–1899 (2005)